Novel Impedance Sensing via Semiconductor Strain Gauge and Magnetic Resonant Coupling for Wireless Force Measurement

Changrong Yang, Guiyun Tian, *Senior Member, IEEE*, Mark Robinson, Qiuping Ma, Lawal Umar Daura, *Member, IEEE*, Emmanuel Tashiwa Ibrahim

Abstract*—Wireless force measurement (WFM) can be used for those scenarios where cable connection and power supply are not available, such as wheel rail force measurement. To enhance the sensitivity and extend the lift-off (the distance between the Tx and Rx) for WFM, this paper introduces a novel approach based on impedance sensing through magnetic resonant coupling (MRC), coupled with a semiconductor strain gauge (SSG), and measured by a developed inductance to digital converter (LDC)-based system. Initially, a simulation was performed to investigate the influence of SSG at various coupling coefficients using parallel-parallel (PP) and series-parallel (SP) MRC topologies. Subsequently, the experiment conducted loading tests on a carbon steel specimen. A traditional strain gauge (SG) was also compared with the SSG in the same experimental set-up. Additionally, the response and sensitivity of the two topologies were analysed at various lift-offs and SSGs. The results demonstrate that the approach based on impedance sensing, MRC, and a miniaturized LDC-based system achieved WFM with high sensitivity and high lift-offs. Both equivalent parallel resistance (R_{Peq}) and resonant frequency (f_{res}) exhibited an excellent linear relationship with the force. The sensitivity in R_{Peq} was found to be relatively stable near the critical coupling region, while f_{res} exhibited only an exponential curve. SSGs affected the optimal lift-off for both PP and SP topologies. The proposed approach is highly suitable for WFM, offering low cost, portability, and fast response advantages.

***Index Terms*—Equivalent parallel resistance, high lift-off, inductance-to-digital converter, impedance sensing, magnetic resonant coupling wireless power transfer, wireless force measurement, resonant frequency.**

I. INTRODUCTION

Wheel-rail contact force measurement in railway vehicle dynamics is significant as it affects running safety and stability [1]. Real-time force monitoring provides crucial parameters such as derailment coefficients and the deterioration quality of track geometry to understand the dynamic performance of railway vehicles [2]. At present, the measurement of wheel-rail contact forces primarily depends on specialized wheelsets equipped with strain gauges (SG), slip rings, or telemetry, since the measurement is conducted on a rotating wheel. However, this method has drawbacks, including strict requirements of drilling holes, complicated signal transmission, and expensive fabrication costs [1]. Some indirect measurement methods have been proposed, including the use of acceleration signal from the axle box and car body to represent wheel-rail vertical and lateral forces, non-contact eddy current sensors and other gap sensors for wheel-rail lateral force measurement [1], [3], [4]. Another approach involves utilizing a space fixed-point strain of wheel web through digital image correlation (DIC) technology [4]. While these methods have significantly improved wheel-rail force measurement, a simple, cost-effective, and wireless method is still needed.

Many scholars have made significant advancements in WFM. Table 1 lists the existing WFM methods, especially for applications on metal components. Radio frequency identification (RFID)-based methods have been broadly applied in WFM based on their excellent capability in power and data transfer [30-33]. A force sensor was integrated with an RFID tag, signal conditioning circuits, and a microcontroller for WFM [30]. The RFID tag harvested energy from an RFID reader to activate the sensor system. Then sensor data was processed by the microcontroller and transmitted wirelessly by the RFID tag's antenna [31]. Yi *et al.* proposed an RFID-based strain-sensing antenna with a patch antenna specially designed with an RFID chip to sense stress [32]. Kuhn *et al.* designed an RFID-based inverted-F antenna for remote deformation assessment on metal components, which depended on the change of the antenna's geometrical size under deformation [33]. Since these methods operate at ultra-high frequency (UHF), signal transmission is based on far-field electromagnetic radiation, allowing communication over long distances, up to several meters. However, RFID readers are usually large, limiting their use in confined spaces. Also, RFID tags operate at high frequencies, and they are more susceptible to electromagnetic interference (EMI) and environmental factors such as temperature and humidity [38]. Apart from far-field RFID-based WFM, substantial research focuses on near-field inductive sensing for WFM [36], [37]. Li *et al.* designed a wireless passive flexible inductor-capacitor (*LC*) strain sensor using aluminium nitride film for rolling bearings where a readout coil connected to a vector network analyser (VNA) was employed to measure the resonant frequency of this *LC* sensor in response to strain, offering the advantages of small size and high resolution [28]. A battery-less and wireless strain sensor made with stretchable silicone rubber and a serpentine coil was presented in [29], which monitored the shift in resonant frequency caused by stomach mobility. Although these methods offer new insights into WFM, the signal readout approach requires an expensive and bulky VNA, which hinders the achievement of low cost and portability. Besides, the measurement time is also prolonged due to the need for frequency sweeping to obtain the resonant frequency [35].

Considering cost, portability and measurement time, a miniaturized, low-cost, and portable measurement system is needed. Our previous research demonstrated the feasibility of utilizing *LC* resonance sensors with an LDC-based measurement system to realize non-contact force measurement [5]. This was accomplished by sensing variations in the electromagnetic properties of the specimen under applied forces. The LDC-based system integrated both the resonant driver and the frequency measurement unit into a single chip, providing advantages such as miniaturization, portability, and low power consumption [6]. The measurement and separation of forces and lift-offs (the distance between the sensor and the test object), were also investigated by the proposed orthogonal *LC* resonance sensor and 8-node isoparametric coordinate transformation, effectively achieving the separation of forces and lift-offs within 14 kN and 2 mm [25]. However, as they relied on electromagnetic induction, their effective lift-offs were restricted to less than 2 mm. This limitation could lead to sensors contacting the measured objects in real-world applications due to vibration or irregular movement, potentially damaging sensors. Therefore, it is necessary to find a way to extend lift-offs. The utilization of wireless power transfer (WPT) concepts can offer a potential solution [7-9].

Wireless power transfer (WPT) is an emerging and promising battery-free technology and has found widespread applications, including electric vehicles (EVs), consumer electronics, implantable medical devices, and the Internet of Things (IoT) [7-9]. The medium-range magnetic resonant coupling WPT (MRC-WPT) [8] consists of a transmitter coil, a receiver coil, and a capacitive compensation network, which has garnered significant attention due to its high transfer efficiency and greater transmission distance compared to other WPT methods. An MRC-WPT system comprises two *LC* tanks—one for the transmitter (Tx) and another for the receiver (Rx). There are four basic compensation topologies: series-series (SS), series-parallel (SP), parallel-series (PS), and parallel-parallel (PP) [9]. Each of them provides unique benefits and can be employed based on the specific requirements of the application to ensure optimal power transfer efficiency and resonance tuning [10]. Most research scholars concentrate on topics related to energy transmission efficiency [11], distance enhancement [12], coil misalignment [13], cross-coupling [14], frequency splitting [15] and smart multi-receiver system [16]. However, there is limited research investigating WPT-based sensing.

In terms of sensing or signal transmission, MRC-WPT can achieve extended measurement distances when not used for energy transfer. Researchers have employed MRC-WPT for wireless force and pressure sensing, as demonstrated by C Zhang *et al*. [17], who developed a wireless triboelectric nanogenerator (TENG) based on MRC-WPT for energy transfer and wireless force and pressure sensing. The force and pressure were detected by the resonant frequency shift and signal amplitude changes induced by a capacitive sensor. C Yang *et al*. [18] introduced an integrated wireless theranostic contact lens for in-situ intraocular pressure sensing which employs a cantilever configuration in the capacitive sensing circuit, enabling ultrasensitive detection of intraocular pressure fluctuations. C. T. Ertsgaard *et al*. [19] utilized resonant WPT coupled to a nanogap capacitor to detect particles in biosensing platforms via changes in the impedance. They analysed PS circuit architecture and optimal coupling regime, including weak coupling, critical coupling, and strong coupling, which affected particle trapping and detection. Furthermore, MRC-WPT technology has been applied for non-destructive testing and evaluation (NDT&E) [20], where multiple resonance responses in frequency splitting were utilized to characterize angular rolling contact fatigue (RCF) cracks in railway tracks by providing distinct features related to various crack parameters, enabling the quantitative analysis of RCF cracks.

This paper demonstrates a novel impedance sensing approach using SSG, MRC, and a developed LDC-based measurement system to achieve WFM and extend the lift-off. The proposed approach employs two *LC* tanks (Rx and Tx) integrated with the SSG and LDC-based system. The SSG is connected to Rx and responds to changes in force, resulting in a change in the impedance of Rx. Through MRC, this change in Rx's impedance is reflected in the impedance of Tx. The use of SSG is a crucial factor due to its high gauge factor compared to metal foil strain gauges, resulting in a relatively significant change in impedance and enhanced sensitivity. The LDC-based system measures the real part (equivalent parallel impedance R_{Peq}) and imaginary part (resonant frequency f_{res}) of Tx's impedance. This approach fully employs the extended distance capability of MRC, the high gauge factor of the SSG, and the low cost and fast response of the developed LDC-based measurement system, achieving significantly longer lift-off measurements compared to the previous work [5], [25].

The achievements of this paper can be summarized as:

1) The high sensitivity of the SSG, transmission characteristics of MRC, and an integrated LDC-based system were utilized to achieve WFM ranging from 2 kN to 14 kN, with a maximum lift-off up to 40 mm. This approach surpasses the limitations of using only an *LC* sensor for force measurement, which has a maximum lift-off of 2 mm. Both the simulation and experimental results showed good agreement.

2) The use of traditional SG and SSG for WFM were compared. The latter exhibited a higher response than the former, approximately 32 times greater for R_{Peq} and 59 times greater for f_{res}.

3) The sensitivity of PP and SP topologies at different lift-offs and SSG values R_{str} was analysed, highlighting that optimal sensitivity is not only related to lift-offs and topologies but also to SSG values. Overall, the SP topology has a more comprehensive working range than the PP topology.

The remainder of the article is organized into four sections. Section II describes the methodology of applying MRC coupled with an SSG for force measurement. Section III presents simulations using LT-Spice to investigate the MRC-based circuit models. In section IV, experimental studies are conducted compare the traditional SG and SSG and PP and SP topologies at various lift-offs and SSGs. The results are then discussed. The final section concludes the work and outlines future work.

Table 1. Comparison of WFM methods, especially for metal applications

Literature	Method	Parameter	Measurement mode	Sensing distance	Cost range (USD)	Limitation
Wu *et al.* [1]	SG, Wheatstone bridge, slip ring	Resistance	Contact	0 mm	> $10,000	Wired connection, complicated signal transmission system
Li *et al.* [28] Lee *et al.* [29]	Stretchable LC strain sensor + Readout coil + VNA	f_{res}	Wireless/passive/ chipless	< 22.5 mm	> $13,000	Unable to apply on metal, expensive measurement device, frequency sweeping
Cui *et al.* [30] Cheng *et al.* [31]	SG + MCU + RFID Antenna + Reader	Resistance	Wireless/passive/ chip	< 5 m	> $2,000	Complicated circuit, and bulky reader, frequency sweeping
Yi *et al.* [32] Kuhn *et al.* [33]	RFID-based strain antenna+ RFID reader	f_{res}	Wireless/passive/ chip	< 2.5 m	> $40,000	Susceptible to EMI and bulky system
Wang *et al.* [4]	Digital image correlation technology	Strain at space-fixed points	Wireless	Tens of cm	> $10,500	Expensive device, complicated image processing
Yang *et al.* [5], [25]	LC resonance sensor + LDC (eddy current effects)	R_{Peq}, f_{res}	Wireless	< 2 mm	< $100	Low lift-off, low sensitivity
This work	SSG (deformation) + MRC + LDC	R_{Peq}, f_{res}	Wireless/passive/ chipless	< 40 mm	< $100	Lift-off interference and misalignment (coupling coefficient)

II. Methodology

This section presents the principle of MRC-based impedance sensing for force measurement. Formulas related to the PP and SP topologies of MRC models are derived.

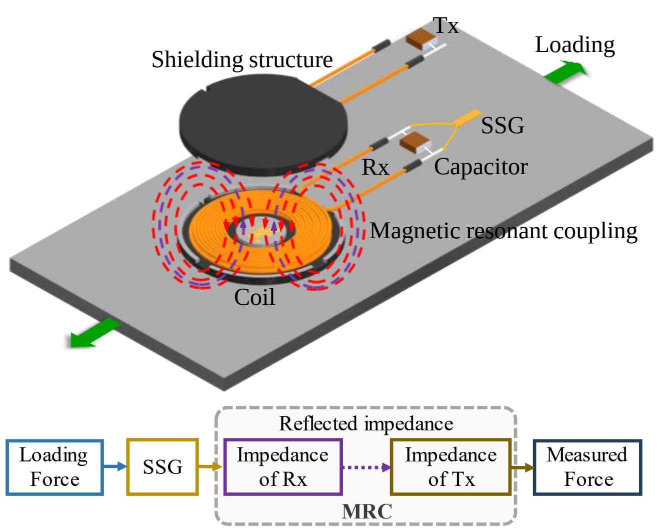

(a) Illustration of MRC-based force measurement

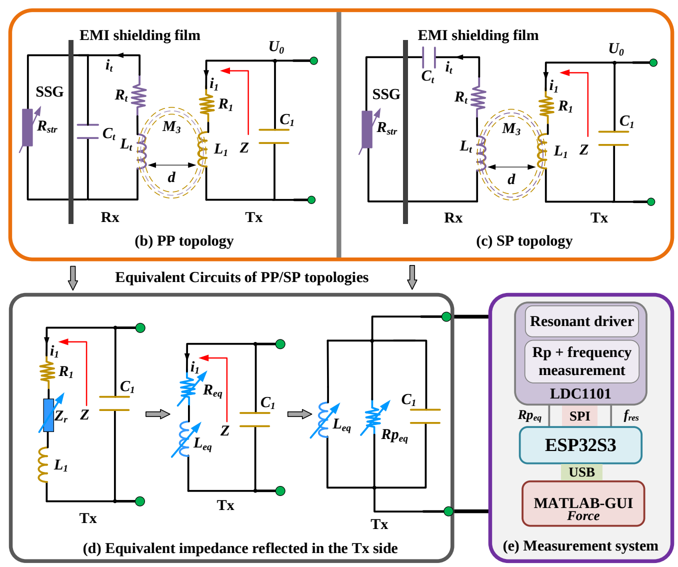

Fig.1. (a) Illustration of magnetic resonance coupling (MRC)-based impedance sensing for force measurement. (b) Parallel-parallel (PP) topology. (c) Serial-parallel (SP) topology. (d) Equivalent impedance reflected in the transmitter (Tx) side. (e) The inductance-to-digital converter (LDC)-based measurement system.

A. Principle of MRC-based Impedance Sensing

As shown in Fig.1 (a), MRC-based impedance sensing utilizes the resistance change in an SSG caused by force, which affects the impedance of Rx. This change is then reflected to the Tx side via magnetic coupling. The Tx is connected to an LDC-based system to measure the equivalent parallel resistance R_{Peq} and resonant frequency f_{res} that are related to the Tx's impedance. As the LDC-based system requires the LC tank to be parallel, the Tx side is configured for a parallel connection. Fig. 1 (b) and (c) show the equivalent circuit models of PP and SP topologies connected to the SSG R_{str}. The only difference is on the Rx side, where the PP topology features a parallel connection between R_{str}, the capacitor C_t, and the equivalent circuit of an inductor coil that includes a series resistance R_t and series inductance L_t. In contrast, in the SP topology, all the components are connected in series. Fig. 1 (d) illustrates how the reflected impedance Z_r couples from the PP/SP topology to the Tx side [23], and the LDC-based measurement system is shown in Fig. 1 (e).

In addition, the presence of metallic materials can cause the coils on the Tx and Rx sides to induce eddy currents in the specimen, which may affect the signal sensing and transmission [21]. It is imperative to minimize the influence of eddy currents. Electromagnetic interference shielding (EMI) structures can suppress these eddy currents by isolating the Tx/Rx coil from metal objects and focusing the magnetic fields between the Tx and Rx coils [22]. This work differs from the previous research, which heavily relied on eddy currents in the specimen to characterize the electromagnetic properties (electrical conductivity σ and permeability μ) in response to forces [5], [25]. However, the intensity of eddy currents is strongly related to the lift-off. An increase in the lift-off results in an exponential decrease in the intensity, causing to a low sensitivity in testing [39]. To address this challenge, we employ an SSG as a force sensor and transform its variation into the impedance change via MRC-WPT. This approach enables wireless sensing and long-distance transmission for force measurement.

B. Formula Derivation of PP/SP Topology

Based on Kirchhoff's circuit laws, the circuits in Fig. 1 can be further derived and simplified. The impedance of Rx (Z_{Rx}) in terms of the PP topology, is derived as follows:

$$\begin{aligned} Z_{Rx} &= \frac{1}{j\omega C_t} // R_{str} + (R_t + j\omega L_t) \\ &= \frac{R_{str}(R_t + j\omega L_t)}{R_{str} + R_t + j\omega L_t + j\omega C_t R_{str}(R_t + j\omega L_t)} \end{aligned} \tag{1}$$

For the SP topology, Z_{Rx} is given as:

$$Z_{Rx} = \frac{1}{j\omega C_t} + R_{str} + (R_t + j\omega L_t) \tag{2}$$

The reflected impedance Z_r is expressed as [23]:

$$Z_r = \frac{\omega^2 M^2}{Z_{Rx}} \tag{3}$$

Where ω is the angular frequency and M is the mutual inductance between the Tx coil and Rx coil, k is the coupling coefficient dependent on the lift-off (the distance between two coils) and M is described as:

$$M = k\sqrt{L_t L_1}\ (0 < k < 1) \tag{4}$$

The impedance of Tx (Z_{Tx}) after combing Z_r together is written as:

$$Z_{Tx} = \frac{1}{j\omega C_1} // (R_1 + j\omega L_1 + Z_r) = \frac{1}{j\omega C_1} // Z \tag{5}$$

Where Z is the equivalent impedance from the Tx coil's point view, it is equal to:

$$Z = R_1 + j\omega L_1 + Z_r = R_1 + j\omega L_1 + \frac{\omega^2 M^2}{Z_{Rx}} \tag{6}$$

For the PP topology, Z is derived as (7):

$$\begin{aligned} Z &= R_1 + j\omega L_1 + \frac{\omega^2 M^2}{\left(R_t + R_{str}(1-\omega^2 L_t C_t)\right)^2 + \omega^2 (L_t + C_t R_{str} R_t)} \Big(R_{str} + R_t + \omega^2 {C_t}^2 R_t {R_{str}}^2 \\ &\qquad + j\omega\left({R_{str}}^2 C_t (1-\omega^2 L_t C_t) - L_t\right)\Big) \\ &= R_1 + \frac{\omega^2 k^2 L_1 L_t}{\left(R_t + R_{str}(1-\omega^2 L_t C_t)\right)^2 + \omega^2 (L_t + C_t R_{str} R_t)} \left(R_{str} + R_t + \omega^2 {C_t}^2 R_t {R_{str}}^2\right) \\ &\qquad + j\omega\left(L_1 + \frac{\omega^2 k^2 L_1 L_t \left({R_{str}}^2 C_t (1-\omega^2 L_t C_t) - L_t\right)}{\left(R_t + R_{str}(1-\omega^2 L_t C_t)\right)^2 + \omega^2 (L_t + C_t R_{str} R_t)}\right) \\ &= R_{eq} + j\omega L_{eq} \end{aligned} \tag{7}$$

Similarly, Z in the SP topology is derived as (8):

$$\begin{aligned} Z &= R_1 + j\omega L_1 + \frac{\omega^2 M^2}{R_{str} + R_t + j\left(\omega L_t - \frac{1}{\omega C_t}\right)} \\ &= R_1 + \frac{\omega^2 k^2 L_1 L_t (R_{str} + R_t)}{(R_{str} + R_t)^2 + \left(\omega L_t - \frac{1}{\omega C_t}\right)^2} + j\omega\left(L_1 - \frac{\omega^2 k^2 L_1 L_t \left(L_t - \frac{1}{\omega^2 C_t}\right)}{(R_{str} + R_t)^2 + \left(\omega L_t - \frac{1}{\omega C_t}\right)^2}\right) \\ &= R_{eq} + j\omega L_{eq} \end{aligned} \tag{8}$$

Thus, the equivalent parallel resistance R_{Peq} of the Tx is:

$$R_{Peq} = \frac{L_{eq}}{R_{eq} C_1} \tag{9}$$

The resonant frequency f_{res} is expressed as:

$$f_{res} = \frac{1}{2\pi\sqrt{L_{eq}C_1}} \tag{10}$$

Equations (1)-(10) illustrate how the resistance of an SSG, R_{str}, affects the impedance of Rx (Z_{Rx}), the reflected impedance Z_r and subsequently the impedance of Tx (Z_{Tx}). The LDC-based system then measures the real and imaginary parts of Z_{Tx}, represented by R_{Peq} and f_{res}, which are then measured by the LDC-based system.

III. Simulation

In this section, circuit modelling was conducted using LT-Spice to investigate the MRC coupling coefficients for PP/SP topologies with and without an SSG, the phenomenon of frequency splitting, and the influence of an SSG on the impedance of Tx.

A. *PP/SP without SSG: Coupling Coefficient and Frequency Splitting*

To investigate the influence of an SSG on MRC circuit models, a model without an SSG was constructed, consisting of only two *LC* tanks: one representing Rx on the left side and the other for Tx on the right side. Rx consisted of a 470 pF capacitor (C_t), a 10 μH inductor (L_t), and a series resistor R_t of 0.5 Ω. Tx had the same components as Rx. Each *LC* tank corresponded to a resonant frequency of 2.3215 MHz. An AC analysis was employed to simulate the impedance-frequency characteristics. The coupling coefficient k was varied from 0 to 0.1 with a step of 0.025, representing changes in the lift-off, while the frequency was swept from 2.15 MHz to 2.5 MHz in 100 Hz increments.

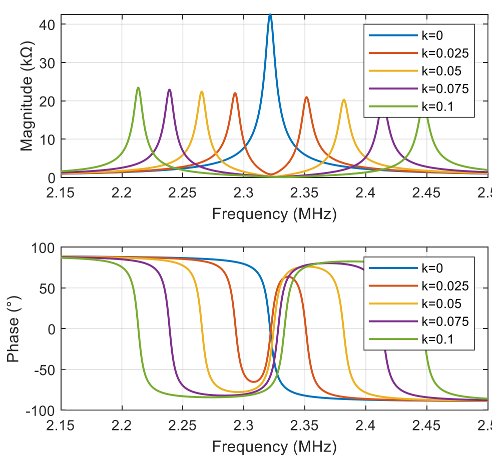

Fig. 2. Impedance of the transmitter (Tx) without a semiconductor strain gauge (SSG).

Fig. 2 illustrates the impedance-frequency characteristic of Z_{Tx} at different coupling coefficients. As the coupling coefficient k increased, indicating a decrease in the distance between Tx and Rx coils, the phenomenon of frequency splitting occurred, leading to variations in the resonant frequency and phase [15]. This phenomenon affected the transmission performance of the system. In a WPT system, frequency splitting should be avoided through careful design, proper parameter selection, and advanced control algorithms in a WPT system [15], [26].

B. *PP/SP with SSG at Different Coupling Coefficients*

Unlike Fig. 2, which did not include an SSG, an SSG with a resistance of 350 Ω, denoted as R_{str}, was added to both the PP and SP topologies, as shown in Fig. 1 (b) and (c). The coupling coefficients and frequency range remained the same as before. The simulation results are presented in Fig. 3 (a) and (b). In contrast to Fig. 2 (b), where frequency splitting was observed, the setups here did not exhibit any frequency splitting. In the PP topology, the magnitude decreased as k increased because the increase in k caused R_{eq} to rise, which in turn lead to a decrease in R_{Peq}. The resonant frequency shifted to the right due to a decrease in L_{eq}. It can be explained by Equation (7) where L_{eq} was smaller than L_1 after the sweeping frequency exceeded the original resonant frequency $f_{res0} = 1/2\pi\sqrt{L_1C_1}$. A similar trend of magnitude was observed in the SP topology. Nevertheless, the resonant frequency remained unchanged, which can be attributed to the fact that L_{eq} in Equation (8) is equal to L_1 at f_{res0}. In both topologies, the phase curves gradually became flat as k continued to rise, and they passed through a common point at f_{res0}. That intersection point was similar to the lift-off point of intersection (LOI) in eddy current testing (ECT) [24].

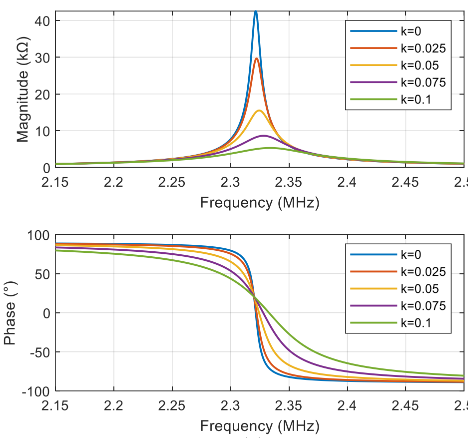

(a)

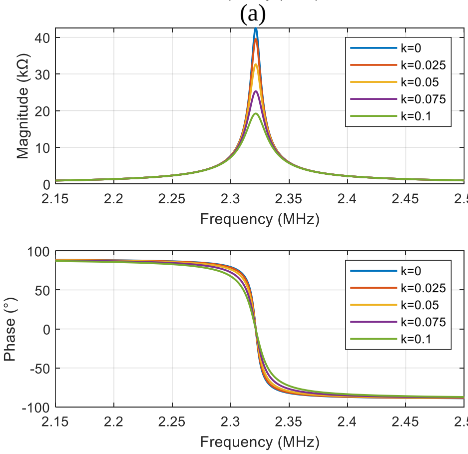

(b)

Fig. 3. Magnetic resonance coupling (MRC)-based circuit modelling: (a) Parallel-parallel (PP)-Impedance of the transmitter (Tx). (b) Serial-parallel (SP) -Impedance of Tx.

C. Variation of SSG R_{str}

The simulation results in the previous sub-section demonstrated that frequency splitting did not occur at the designated coupling coefficients for both PP and SP topologies after adding the SSG. To understand the influence of the SSG on the Tx's impedance, the changes in SSG resistance for both topologies were simulated. Since the SSG resistance value was proportional to the force, R_{str} was set to vary from 350 Ω to 400 Ω with a step of 10 Ω, imitating that an increasing force was applied to the SSG. The coupling coefficient k was fixed at 0.1. Fig. 4 (a) and (b) illustrate the change in the impedance of the Tx due to R_{str}. As the R_{str} increased, the magnitude decreased in the PP topology but increased in the SP topology. The maximum value of the magnitude was extracted for both topologies. The resonant frequency corresponding to the maximum magnitude did not change because of the weak coupling with k of 0.1. In this coupling range, the contribution of the change in R_{str} for the imaginary part could be neglected.

The phase information of both topologies remained almost unchanged with the variation of R_{str}. Fig. 5 presents a linear relationship between the maximum of magnitude and the SSG in the PP and SP topologies, illustrating that employing an SSG coupled to MRC models for WFM is feasible.

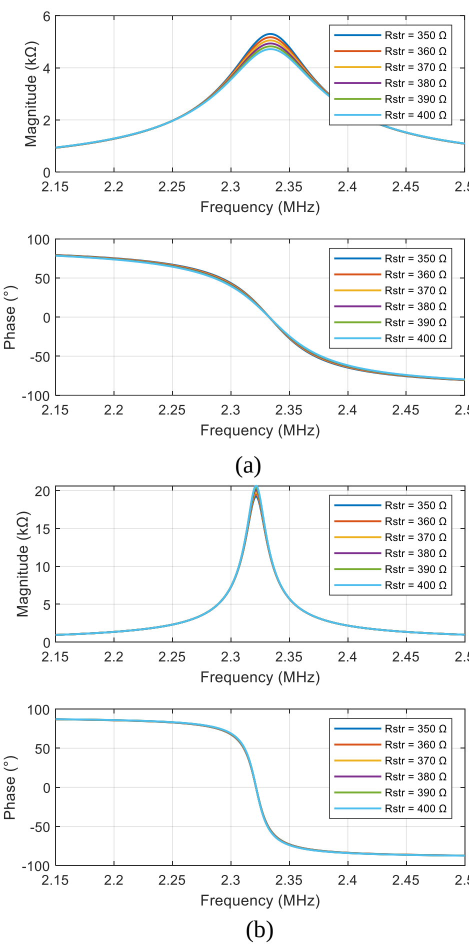

Fig. 4. Variation of R_{str} for the influence of the transmitter (Tx)'s impedance: (a) Parallel-parallel (PP) topology. (b) Serial-parallel (SP) topology.

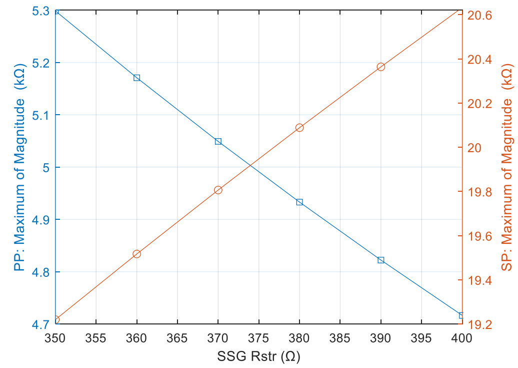

Fig. 5. The extracted maximum of magnitude against the semiconductor strain gauge (SSG) R_{str}.

IV. EXPERIMENTAL STUDY AND RESULTS

This section describes the experimental study and results, including the experimental set-up, the measurement system based on LDC1101 and ESP32S3 for R_{Peq} and f_{res}, the SSG, MRC components, the comparison of a traditional SG and SSG, tensile testing results for PP/SP topologies with different SSGs and lift-offs, and a subsequent discussion.

A. Experimental Set-up

The experimental set-up included a testing machine INSTRON 3369, an LDC1101-ESP32S3 measurement system, an SSG, two MRC LC tanks, and a carbon steel C50 dog-bone specimen, as shown in Fig. 6 (a) and (b). The testing machine was used to load the specimen in line with the pre-configuration. Here, a 2 kN pre-load was applied to remove any slack resulting from the grips, ensuring accurate and reliable measurements [27]. To implement repeatability tests, the loading force was kept within the elastic region. The loading then increased from 2 kN to 14 kN and was held for 30 seconds, followed by unloading from 14 kN back to 2 kN, as shown in Fig. 6 (c). The speed of the crosshead was set at 0.5 mm/min.

Unlike simulations and most systems that rely on a bulky and expensive VNA to obtain the maximum of magnitude and resonant frequency through frequency sweeping [19], [20], our system can directly measure the impedance characteristics in the resonant state, specifically R_{Peq} and f_{res}. It offered low-cost, portable, and time-saving benefits. The system consisted of an inductance-to-digital converter LDC1101 (Texas Instruments) [40], which supported an LC tank with a f_{res} range of 500 kHz to 10 MHz, an R_{Peq} range of 0.75 kΩ to 96 kΩ, and a 180 kSPS conversion rate. The LDC1101 was controlled by an IoT-level microcontroller, the ESP32S3 (Espressif Systems), via 4-wire SPI communications. Both R_{Peq} and f_{res} measurements achieved a 16-bit resolution. The mechanism of the readout system is the LDC-based system outputs a high-frequency pulse signal to drive the Tx, causing it to resonate at its resonant frequency. The resonant frequency f_{res} is then measured by counting the number of cycles of a reference frequency, similar to the principle of frequency meter. Meanwhile, R_{Peq} is measured by regulating the oscillation amplitude in a closed-loop configuration to a constant level while monitoring the energy dissipated by the Tx [34]. Any change in R_{eq} and L_{eq} incurred by the SSG due to force will lead to a change in R_{Peq} and f_{res}.

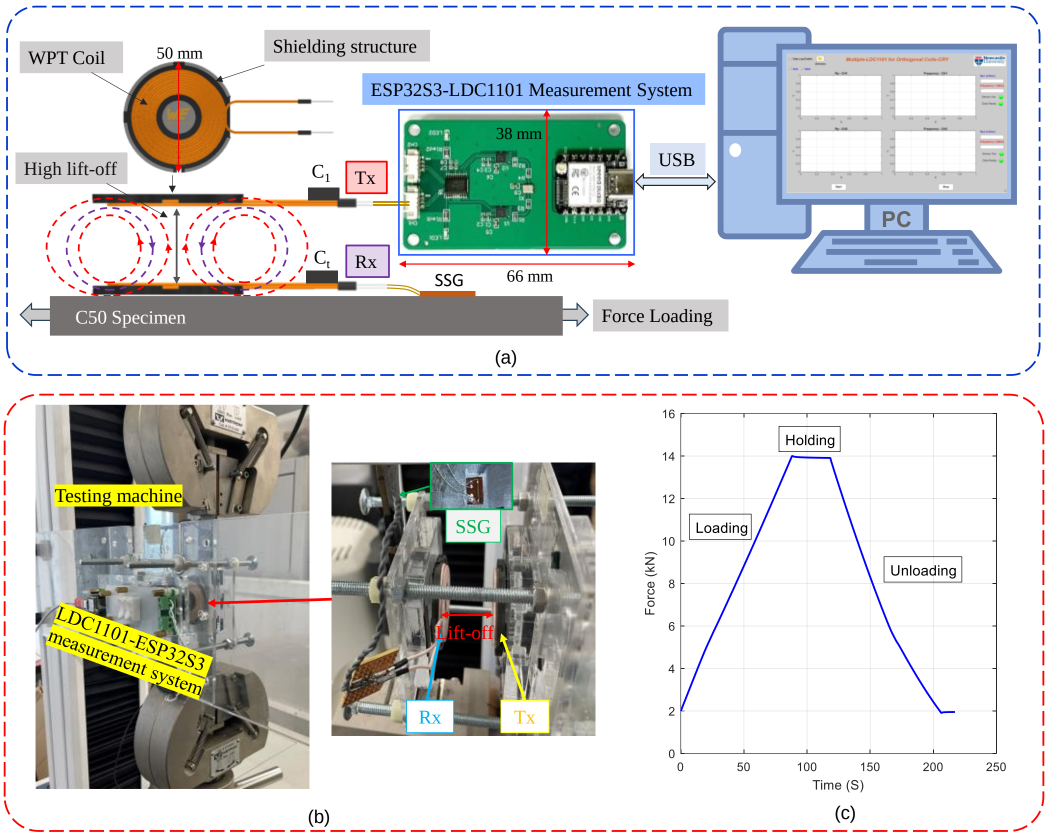

Fig. 6. (a) System diagram of magnetic resonance coupling (MRC)-based impedance change for force measurement. (b) Experimental set-up. (c) Force loading, holding, and unloading curves.

An SSG force sensor (6 mm x 4 mm x 0.04 mm, manufactured by BENGBU KECHUANG SENSOR CO. LTD) with a nominal value of 350 Ω and a gauge factor of 130 was used, which is significantly higher than that of a traditional metal foil strain gauge. The two *LC* tanks had identical coils and capacitors. The inductance of both Tx and Rx coils (Würth Elektronik 760308100141, 50 mm in diameter) was 10 µH. The coil traces were made using Litz wires to reduce skin-depth effects at high frequencies. The coils were wounded on a shielding structure to minimize EMI interference and to focus the magnetic field, thereby enhancing the sensing and transmission distance. Two identical 470 pF capacitors were used with both coils, generating an initial resonant frequency of 2.3215 MHz in air. The SSG was bonded to the centre of the specimen using Cyanoacrylate adhesive after the surface of the specimen was cleaned. The wires from the SSG were then connected to the Rx in parallel or series to form PP or SP topologies. The *LC* tank in the Tx was in parallel to the inputs of LDC1101. Both *LC* tanks were aligned on a supporting plate, and the lift-off could be adjusted by screwing the nuts. The collected data were transmitted to the MATLAB-based GUI via USB from the ESP32S3, and the data were processed using MATLAB. Before testing, the specimen was pre-loaded, and then the system conducted the testing according to the settings.

B. Comparison of WFM using the traditional SG and SSG

A traditional metal foil strain gauge (SG, BF350-3AA, 7.4 mm x 4.1 mm x 0.032 mm) with a nominal value of 350 Ohm and gauge factor of 2 was used to compare with the SSG. The experimental set-up was the same for the two cases. The lift-off was set to 25 mm. Fig. 6 (c) presents the input force, and Fig. 7 (a) and (b) show the sensing results for two types of SGs. The results at the loading stage were analyzed. Both exhibited an inverse proportional relationship with the input force. Table 2 provides a comparison of several key factors, including the variation in R_{Peq} and f_{res}, as well as the fitting factor R^2. The SSG exhibited a higher response than the traditional SG, approximately 32 times greater for ΔR_{Peq} and 59 times greater for Δf_{res}. Besides, R^2 for SSG was larger than the SG. In summary, the SSG demonstrates better sensitivity and linearity than the traditional SG due its larger gauge factor.

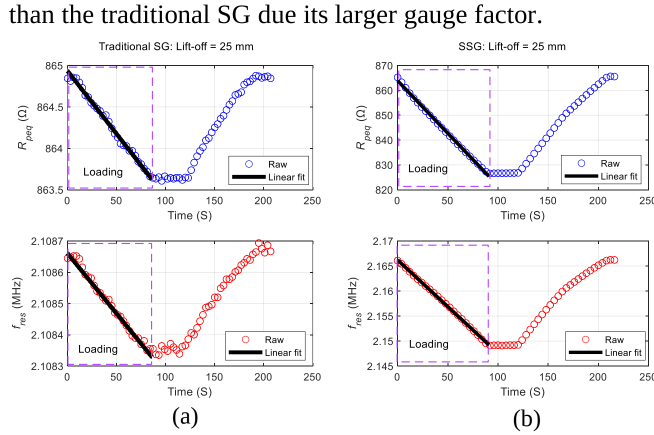

Fig. 7. Experimental results of (a) traditional strain gauge (SG) and (b) semiconductor strain gauge (SSG).

Table 2. Comparison of traditional strain gauge (SG) and semiconductor strain gauge (SSG) at the loading stage.

	Traditional SG	SSG
$\lvert \Delta R_{Peq} \rvert$	1.22 Ω	38.69 Ω
$\lvert \Delta f_{res} \rvert$	289.43 Hz	16988.72 Hz
R^2-R_{Peq}	0.9924	0.9982
R^2-f_{res}	0.9897	0.9992

C. PP/SP Topology with SSG for Force Measurement at Different Lift-offs

PP and SP topologies with a 350 Ω SSG were applied in the experiment respectively. Each was tested at a different lift-off. All tests were repeated three times to obtain the average of measurement values. Fig. 8 shows the measured R_{Peq} and f_{res} of the PP topology during force loading, holding, and unloading, with the lift-off varying from 25 mm to 40 mm. It was observed that R_{Peq} decreased as the force increased, which aligned well with the simulation results. Furthermore, R_{Peq} remained almost constant during force holding and increased during the force unloading. The resonant frequency f_{res} also followed the R_{Peq} curves but tended to deteriorate when the lift-off exceeded 30 mm. The change of R_{Peq} and f_{res} with force was explained by Equations (7), (9), and (10), where R_{str} increased with the loading force, resulting in an increase in R_{eq} and L_{eq}, which in turn decreased R_{Peq} and f_{res}, and vice versa. R_{Peq} outperformed f_{res} because changes in SSG values primarily contributed to the real part of the impedance. R_{Peq} and f_{res}, along with the corresponding input force during the loading phase, were then extracted. Fig. 10 (a) and (b) show the curves of R_{Peq} and f_{res} after subtracting the first measured value. A strong linear relationship was observed between them, particularly for R_{Peq}. The absolute sensitivity at various lift-offs is depicted in Fig. 11 (a) and (b), indicated by the blue curve. The sensitivity of R_{Peq} differed from f_{res}, which decreased exponentially as the lift-off increased. The sensitivity in R_{Peq} exhibited a convex pattern, reaching a peak value of 5.5 Ω/kN when the lift-off was approximately 33 mm, indicating that the system was operating in the optimal coupling range due to critical coupling [19]. Furthermore, near the critical coupling region, the sensitivity tended to stabilize, which indicated that operating the Tx and Rx in this region can enhance robustness. In the PP topology with a 350 Ω SSG, it was noteworthy that the minimum lift-off was 25 mm because R_{Peq} approached the lower limit of the measurement system.

For the SP topology with the same SSG, similar tests were conducted at lift-offs of 10 mm, 15 mm, 20 mm, and 25 mm. The lift-off configuration was different from that of the PP topology, as it was adjusted to consider the effective working range of the measurement system. Fig. 9 shows the experimental results of SP topology for force measurement. The curves of the SP topology exhibited a reverse trend compared to the PP topology, which was consistent with the simulation results. Here, both R_{Peq} and f_{res} increased with the force, remained constant when the input force was steady, and decreased as the force decreased. This was explained by Equations (8), (9), and (10), where R_{str} increased with the loading force, leading to a decrease in R_{eq} and L_{eq}, which in turn increased R_{Peq} and f_{res}. Fig. 10 (c) and (d) present the curves of R_{Peq} and f_{res} versus force during the loading stage. Similar to the PP topology, the sensitivity curves in Fig. 11 (c) and (d), indicated by the blue curve, show that R_{Peq} reached a peak value of 6.9 Ω/kN at a lift-off of 10 mm, while f_{res} varied exponentially with the lift-off.

D. Influence of Different SSGs

The influence of different SSGs on the working range and sensitivity was investigated. An additional SSG with a resistance value of 120 Ω was adopted, and similar lift-off tests were carried out. The sensitivity at each lift-off was obtained and plotted in Fig. 11, shown by the red curves. It was observed that different SSGs corresponded to a different working range for R_{Peq} and f_{res}. Since the SSG was a resistive sensor, the sensitivity curve for R_{Peq} performed better compared to f_{res}. The latter was more susceptible to lift-off variations, showing better sensitivity at low lift-offs. However, the former was strongly dependent on the coupling range. In the PP topology, R_{Peq} reached optimal sensitivity at lift-off of 15 mm for a 120 Ω SSG, while for a 350 Ω SSG, its optimal sensitivity appeared at 33 mm. This was because the SSG changed the impedance of the entire system and altered the optimal working range. In the SP topology, a similar phenomenon was observed, but there was a wide overlap in the entire lift-off range for both R_{Peq} and f_{res}.

E. Discussion

The MRC-based impedance sensing for WFM utilizes the characteristics of MRC and high gauge factor of SSGs, as well as the integrated LDC-based measurement system. It transforms the change in SSG into the impedance of the Rx, and then into the impedance of the Tx by the reflected impedance. This approach fully combines the advantages of MRC and overcome the lift-off limitations, achieving the force measurement at high lift-offs. To some extent, the introduction of SSGs effectively avoids the occurrence of frequency splitting, which may have negative effects on measurement performance. Since the SSG is a resistive sensor, its primary impact is on the real part of the impedance, with minimal effect on the imaginary part, particularly at high lift-offs. This can be explained why R_{Peq} exhibited a good quality in contrast with f_{res} during the testing. SSGs in the PP and SP topologies demonstrate distinct influences, affecting the working range, optimal lift-off, and maximum sensitivity. Essentially, the proportion of SSGs in PP and SP topologies is closely associated with the original impedance without connecting any SSGs. When the SSG value is relatively small compared to the original impedance, its impact is more pronounced in the PP topology rather than the SP topology, and vice versa. The LDC1101-based system is a miniaturized device which contains the function of driving Tx and detecting R_{Peq} and f_{res}. However, there are indeed some limitations, such as R_{Peq} needing to be greater than 750 Ω and the resonant frequency of the LC tank being limited to the range of 500 kHz to 10 MHz. These limitations potentially impact the optimal performance of the components. The Tx and Rx coils utilized in the work are

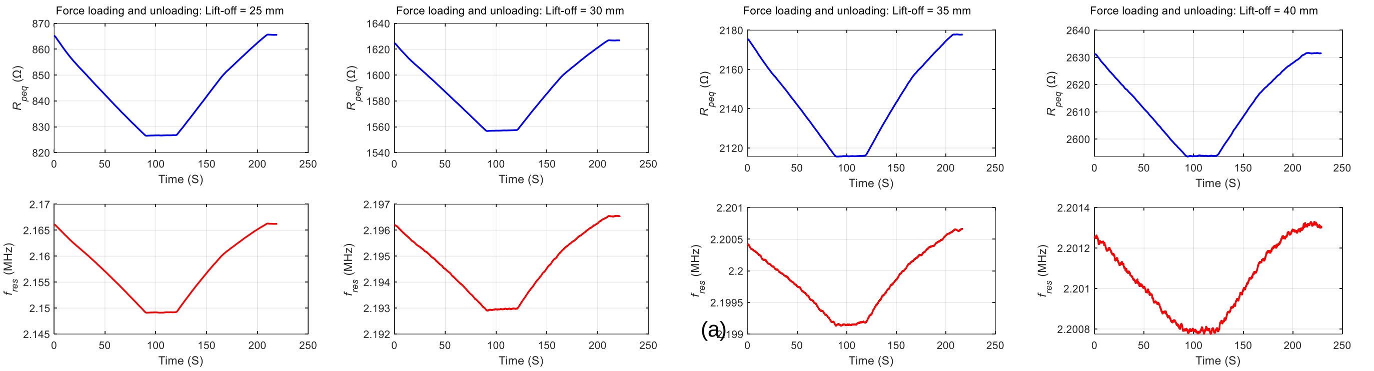

(a) (b) (c) (d)

Fig. 8. Experimental results of parallel-parallel (PP) topology for force measurement at lift-offs: (a) 25 mm. (b) 30 mm. (c) 35 mm. (d) 40 mm.

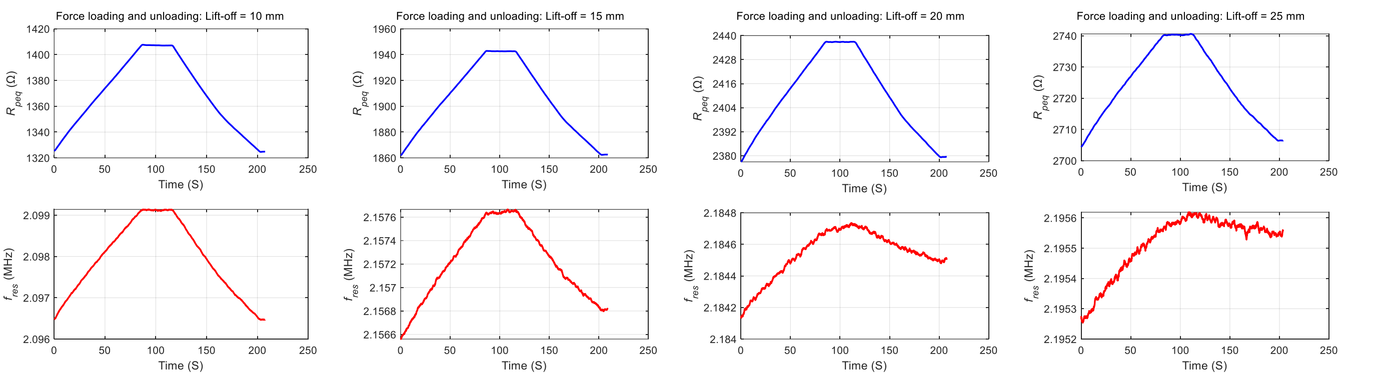

(a) (b) (c) (d)

Fig. 9. Experimental results of serial-parallel (SP) topology for force measurement at lift-offs: (a) 10 mm. (b) 15 mm. (c) 20 mm. (d) 25 mm.

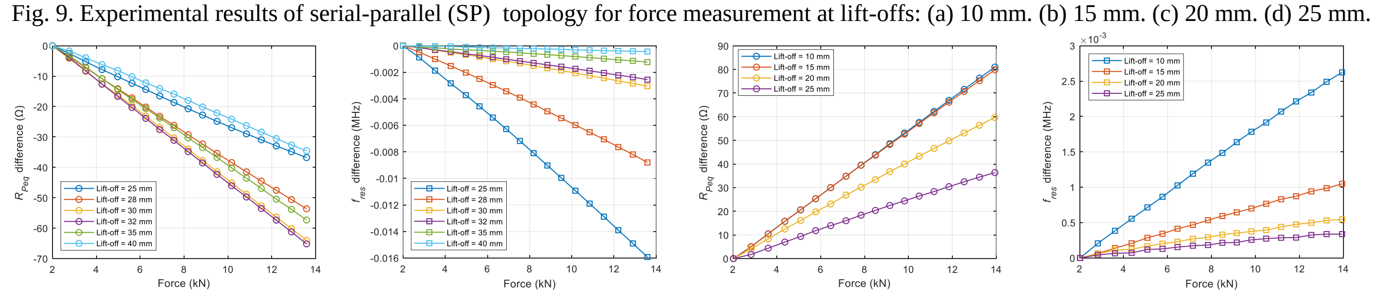

(a) (b) (c) (d)

Fig. 10. Measurement parameters of parallel-parallel (PP)/serial-parallel (SP) topology against loading forces: (a) PP: Equivalent parallel resistance (R_{Peq}) difference versus loading force. (b) PP: Resonant frequency (f_{res}) difference versus loading force. (c) SP: R_{Peq} difference versus loading force. (b) SP: f_{res} difference versus loading force.

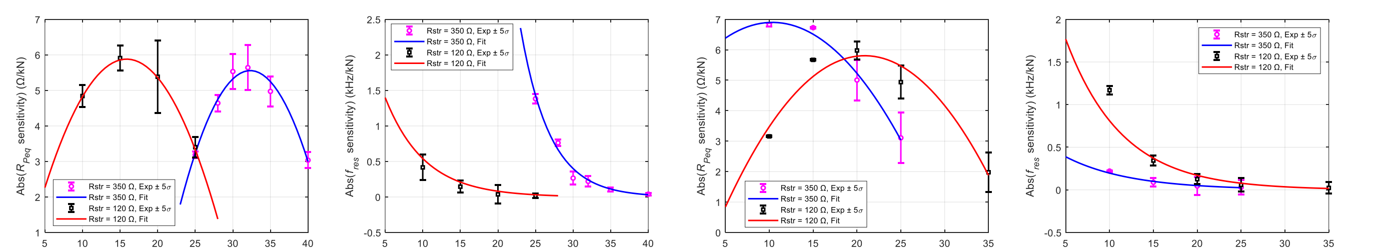

(a) (b) (c) (d)

Fig. 11. Absolute sensitivity against lift-off for parallel-parallel (PP)/serial-parallel (SP) topologies with semiconductor strain gauges (SSGs) of 350 Ω and 120 Ω, with error bars set at five standard deviations (5σ): (a) PP: Equivalent parallel resistance (R_{Peq}). (b) PP: Resonant frequency (f_{res}). (c) SP: R_{Peq}. (d) SP: f_{res}.

ready-made products which can be specially designed to suit the application environment, including curved surfaces, by employing flexible PCB technology. The current method for WFM was affected by the lift-off interference and misalignment between the Rx and Tx coils, which vary coupling coefficients. There may be a method to compensate for these changes by adding an additional *LC* tank measure lift-off.

This paper, primarily focus on the measurements conducted at room temperature, investigating the system's performance under varying MRC topologies, lift-offs and SSGs. However, the temperature variations do affect the system by causing changes in the SSG and inductance of *LC* tanks, ultimately leading to shifts of the f_{res} and R_{Peq}. The following strategies can be implemented to minimize temperature drift. For SSG, a temperature drift curve can be obtained first, and an algorithm will be designed to compensate the change. For inductance variations, since we used COG/NPO capacitors, which have a very low temperature coefficient, the temperature effect on capacitance can be ignored. To address inductance variation due to temperature, another *LC* tank can be added as a reference since the developed LDC1101-ESP32S3 system contains two channels. By obtaining the difference between the transmitter and the reference *LC* tanks, the temperature effects can be minimized.

The range of force in this work was 2 kN to 14 kN due to the elastic region of the carbon steel specimen. This measurement range can be scaled up or down to vary the types of strain gauges according to the testing conditions. Further enhancement of robustness in the proposed system will consider packaging the *LC* tanks and the measurement system such as using epoxy potting compound which is temperature/humidity-resistant, electromagnetic interference shielding, and compensation algorithm for temperature and lift-off variations. The power consumption of LDC1101 and ESP32S3 at the active mode can consume up to tens of milliwatts. Properly entering the low power mode when not performing testing is beneficial to save the energy.

There is always a trade-off between sensitivity, lift-off, topologies, SSG values, and coil shapes. These factors should be carefully selected to maximise the measurement performance.

V. Conclusion and Future Work

In this paper, we proposed a novel WFM approach based on impedance sensing using an SSG and MRC. This method leverages the high sensitivity of the SSG, the transmission characteristics of MRC, and the miniaturized LDC-based impedance measurement system to achieve WFM with enhanced sensitivity at high lift-offs. It offers the benefits of low cost, portability, and fast response, while also overcoming the lift-off limitations inherent in traditional *LC* resonance sensors that rely on eddy current effects.

A comparative study between a traditional SG and SSG for WFM was conducted, demonstrating that the SSG exhibited significantly higher sensitivity, with ΔR_{Peq} being 32 times greater and Δf_{res} being 59 times greater compared to the traditional SG. Both PP and SP topologies with different SSGs and lift-offs were studied through simulations and experiments. The results demonstrated both topologies were effective for WFM at high lift-offs. Specifically, for an SSG of 350 Ω, the PP topology displayed a sensitivity of 3 Ω/kN at a lift-off of 40 mm, while the SP topology presented the same sensitivity at a lift-off of 25 mm. Both R_{Peq} and f_{res} exhibited an excellent linear relationship with input force. It was found that the sensitivity in R_{Peq} revealed a convex pattern, where it tended to stabilize near the critical coupling region, indicating that operating the Tx and Rx in this region can enhance robustness. In contrast, the sensitivity in f_{res} exhibited an exponential relationship. The SSG influenced the optimal lift-off for both PP and SP topologies. Overall, each topology has its advantages and disadvantages, allowing for customization based on specific application needs.

Although the proposed approach is influenced by lift-off interference, misalignment between the Rx and Tx coils, and inherent performance of the LDC-based system, it offers new insights into measuring forces on rotating mechanical components, such as wheel-rail contact force. By attaching an SSG and Rx to wheel areas most susceptible to external impacts, while using a Tx installed on the bearing box, wireless wheel-rail force measurement can be achieved. Additionally, its application can be extended to structural health monitoring of critical infrastructure such as bridges, pipeline, and buildings where power supply and cable connection are unavailable. Moreover, there is potential to integrate this technology with other types of sensors. For instance, SSG can be replaced with capacitive or inductive sensors to monitor various parameters, such as temperature, pressure, humidity, and structural defects. This integration could provide a comprehensive multi-sensor system capable of real-time environmental and structural health monitoring.

Future work will focus on the reduction of the size of MRC *LC* tanks, directional coupling, compensation of lift-off variations and temperature shifts, and IoT application on wheel-rail contact force monitoring.

References

[1] P. Wu, F. Zhang, J. Wang *et al.*, "Review of wheel-rail forces measuring technology for railway vehicles," *Advances in Mechanical Engineering*, vol. 15, no. 3, 2023.

[2] S. Walther, S. Müller, R. Renggli *et al.*, "Prediction of wheel-rail contact forces using simple onboard monitoring system and machine learning," *Proceedings of the Institution of Mechanical Engineers, Part F: Journal of Rail and Rapid Transit*, vol. 237, no. 5, pp. 553-562, 2022.

[3] R. Gadhave, and N. S. Vyas, "Rail-wheel contact forces and track irregularity estimation from on-board accelerometer data," *Vehicle System Dynamics*, vol. 60, no. 6, pp. 2145-2166, 2022.

[4] X. Wang, Z. Lu, J. Wei *et al.*, "Wheel-Rail Contact Forces Monitoring Based on Space Fixed-Point Strain of Wheel Web and DIC Technology," *Advances in Condition Monitoring and Structural Health Monitoring*, Lecture Notes in Mechanical Engineering, pp. 295-304, 2021.

[5] C. Yang, G. Tian, M. Robinson *et al.*, "Wheel-Rail Force Measurement Based on Wireless LC Resonance Sensing," *IEEE Sensors Journal*, vol. 23, no. 15, pp. 17470-17479, 2023.

[6] TI. "LDC1612/4 Datasheet," https://www.ti.com/lit/ds/symlink/ldc1614.pdf.

[7] M. Abou Houran, X. Yang, and W. Chen, "Magnetically Coupled Resonance WPT: Review of Compensation Topologies, Resonator Structures with Misalignment, and EMI Diagnostics," *Electronics*, vol. 7, no. 11, 2018.

[8] W. Liu, K. T. Chau, X. Tian *et al.*, “Smart wireless power transfer — opportunities and challenges,” *Renewable and Sustainable Energy Reviews,* vol. 180, 2023.
[9] Z. Zhang, H. Pang, A. Georgiadis *et al.*, “Wireless Power Transfer—An Overview,” *IEEE Transactions on Industrial Electronics,* vol. 66, no. 2, pp. 1044-1058, 2019.
[10] J. Wang, M. Leach, E. G. Lim, Z. Wang, and Y. Huang, "Investigation of magnetic resonance coupling circuit topologies for wireless power transmission," *Microwave and Optical Technology Letters,* vol. 61, no. 7, pp. 1755-1763, 2019.
[11] Y. Liu, and H. Feng, “Maximum Efficiency Tracking Control Method for WPT System Based on Dynamic Coupling Coefficient Identification and Impedance Matching Network,” *IEEE Journal of Emerging and Selected Topics in Power Electronics,* vol. 8, no. 4, pp. 3633-3643, 2020.
[12] W. Lee, and Y.-K. Yoon, “Wireless Power Transfer Systems Using Metamaterials: A Review,” *IEEE Access,* vol. 8, pp. 147930-147947, 2020.
[13] I. Cortes and W.-j. Kim, "Lateral Position Error Reduction Using Misalignment-Sensing Coils in Inductive Power Transfer Systems," *IEEE/ASME Transactions on Mechatronics*, vol. 23, no. 2, pp. 875-882, 2018.
[14] M. Fu, T. Zhang, X. Zhu *et al.*, “Compensation of Cross Coupling in Multiple-Receiver Wireless Power Transfer Systems,” *IEEE Transactions on Industrial Informatics,* vol. 12, no. 2, pp. 474-482, 2016.
[15] J. Liu, C. Wang, X. Wang *et al*., “Frequency Splitting and Transmission Characteristics of MCR-WPT System Considering Non-Linearities of Compensation Capacitors,” *Electronics,* vol. 9, no. 1, 2020.
[16] Y.-J. Kim, D. Ha, W. J. Chappell *et al.*, “Selective Wireless Power Transfer for Smart Power Distribution in a Miniature-Sized Multiple-Receiver System,” *IEEE Transactions on Industrial Electronics,* vol. 63, no. 3, pp. 1853-1862, 2016.
[17] C. Zhang, J. Chen, W. Xuan *et al.*, “Conjunction of triboelectric nanogenerator with induction coils as wireless power sources and self-powered wireless sensors,” *Nat Commun,* vol. 11, no. 1, pp. 58, Jan 2, 2020.
[18] C. Yang, Q. Wu, J. Liu *et al.*, “Intelligent wireless theranostic contact lens for electrical sensing and regulation of intraocular pressure,” *Nat Commun,* vol. 13, no. 1, pp. 2556, May 17, 2022.
[19] C. T. Ertsgaard, M. Kim, J. Choi *et al.*, “Wireless dielectrophoresis trapping and remote impedance sensing via resonant wireless power transfer,” *Nat Commun,* vol. 14, no. 1, pp. 103, Jan 6, 2023.
[20] L. U. Daura, and G. Y. Tian, “Characterization of Angular RCF Cracks in a Railway Using Modified Topology of WPT-Based Eddy Current Testing,” *IEEE Transactions on Industrial Informatics,* vol. 19, no. 4, pp. 5612-5622, 2023.
[21] L. Dong, L.-F. Wang, and Q.-A. Huang, “Effects of Metal Plane in LC Passive Wireless Sensors,” *IEEE Sensors Letters,* vol. 2, no. 1, pp. 1-3, 2018.
[22] J. Kim, J. Kim, S. Kong *et al.*, “Coil Design and Shielding Methods for a Magnetic Resonant Wireless Power Transfer System,” *Proceedings of the IEEE,* vol. 101, no. 6, pp. 1332-1342, 2013.
[23] P. K. Sahu, S. Jena, S. Behera *et al.*, “Wireless power transfer topology analysis for inkjet-printed coil,” *Open Engineering,* vol. 12, no. 1, pp. 373-380, 2022.
[24] M. Lu, X. Meng, R. Huang *et al.*, “Lift-off invariant inductance of steels in multi-frequency eddy-current testing,” *NDT & E International,* vol. 121, 2021.
[25] C. Yang *et al.*, "Measurement and separation of forces and lift-offs employing an inductance-to-digital converters (LDC)-based orthogonal LC resonance sensor," *NDT & E International,* vol. 144, 2024.
[26] Y.-L. Lyu *et al.*, "A Method of Using Nonidentical Resonant Coils for Frequency Splitting Elimination in Wireless Power Transfer," *IEEE Transactions on Power Electronics,* vol. 30, no. 11, pp. 6097-6107, 2015.
[27] A. Sharma, Y. Morisada, T. Nagaoka, and H. Fujii, "Influence of the number of FSP passes on the strength-ductility synergy of cold-rolled spark plasma sintered pure aluminum," *Journal of Manufacturing Processes,* vol. 79, pp. 296-304, 2022.
[28] M. Li, L. Zhang, H. Dong et al., “Wireless Passive Flexible Strain Sensor Based on Aluminium Nitride Film,” *IEEE Sensors Journal,* vol. 22, no. 4, pp. 3074-3079, 2022.
[29] K. J. Lee, N. Chou, and S. Kim, “A Batteryless, Wireless Strain Sensor Using Resonant Frequency Modulation,” *Sensors (Basel),* vol. 18, no. 11, Nov 15, 2018.
[30] L. Cui, Z. Zhang, N. Gao et al., “Radio Frequency Identification and Sensing Techniques and Their Applications-A Review of the State-of-the-Art,” *Sensors (Basel),* vol. 19, no. 18, Sep 17, 2019.
[31] X. Cheng, Y. Yu, L. Wang et al., “Wireless stress measurement on metal surface based on passive integrated RFID sensor tag,” in 2021 *IEEE International Instrumentation and Measurement Technology Conference (I2MTC)*, 2021, pp. 1-6.
[32] X. Yi, T. Wu, Y. Wang, and M. M. Tentzeris, “Sensitivity modeling of an RFID-based strain-sensing antenna with dielectric constant change,” IEEE Sensors Journal, vol. 15, no. 11, pp. 6147-6155, 2015.
[33] M. F. Kuhn, G. P. Breier, A. R. Dias, and T. G. Clarke, “A novel RFID-based strain sensor for wireless structural health monitoring,” Journal of Nondestructive Evaluation, vol. 37, no. 2, pp. 1-10, 2018.
[34] T. Instruments, "LDC1101 1.8 V High-Resolution, High-Speed Inductance-to-Digital Converter," LDC1101, pp. 1-58, 2016.
[35] M. Masud, P. Vazquez, M. R. U. Rehman *et al.*, “Measurement Techniques and Challenges of Wireless LC Resonant Sensors: A Review,” *IEEE Access,* vol. 11, pp. 95235-95252, 2023.
[36] Q.-A. Huang, L. Dong, and L.-F. Wang, “LC Passive Wireless Sensors Toward a Wireless Sensing Platform: Status, Prospects, and Challenges,” *Journal of Microelectromechanical Systems,* vol. 25, no. 5, pp. 822-841, 2016.
[37] H. Nesser, H. A. Mahmoud, and G. Lubineau, “High-Sensitivity RFID Sensor for Structural Health Monitoring,” *Adv Sci (Weinh)*, pp. e2301807, Jul 5, 2023.
[38] Z. Ye, M. Yang, Y. Ren *et al.*, “Review on Recent Advances and Applications of Passive Harmonic RFID Systems,” *IEEE J Radio Freq Identif,* vol. 7, pp. 118-133, 2023.
[39] B. Feng, S. Xie, L. Xie *et al.*, “Analysis of the Lift-Off Effect in Motion-Induced Eddy Current Testing Based on Semi-Analytical Model,” *IEEE Transactions on Instrumentation and Measurement,* vol. 73, pp. 1-8, 2024.
[40] Instruments T. LDC1101 1.8 V High-Resolution, High-Speed Inductance-to-Digital Converter. LDC1101. 2016 Oct 31:1-58.

Changrong Yang received thea B.Sc. degree in measurement and control technology and instruments from Southwest Petroleum University (2013-2017), Chengdu, China, and the M.Sc. degree in instrument science and technology at University of Electronic Science and Technology of China (2017-2020), Chengdu, China. He is currently pursuing the Ph.D. degree in electrical and electronic engineering from School of Engineering, Newcastle University, Newcastle Upon Tyne, U.K. His research interests include wireless LC resonant sensing for force measurement.

Gui Yun Tian (Senior Member, IEEE) received the B.Sc. degree in metrology and instrumentation and M.Sc. degree in precision engineering from the University of Sichuan, Chengdu, China, in 1985 and 1988, respectively, and the Ph.D. degree from the University of Derby, Derby, U.K., in 1998. He is a Chair Professor in Sensor Technologies at Newcastle University, Newcastle upon Tyne, U.K. Currently, He is also an adjunct professor with the School of Automation Engineering, University of Electronic Science and Technology of China. He has coordinated several research projects from the Engineering and Physical Sciences Research Council (EPSRC), Royal Academy of Engineering and FP7, on top of this he also has good collaboration with leading industrial companies such as Airbus, Rolls Royce, BP, Power, Network rail and TWI among others.

Mark Robinson is the Professor of Rail Systems Engineering, in the School of Engineering, Newcastle University and Technologies lead for the Newcastle University Centre of Excellence for Mobility and Transport. He is also Director of Newcastle Centre for Rail Research (NewRail) and Fellow of the Institute of Materials, Minerals and Mining (FIMMM), Chartered Engineer (CEng) and Chartered Scientist (CSci). His main research interests include asset management, infrastructure and rail vehicle maintenance, railway technology and inspection and monitoring techniques. He has won awards for vehicle joining technologies and use of composites for lightweighting of rail vehicles. He is Vice

Chairperson of the Union of International Railway's (UIC) International Rail Research Board (IRRB) responsible for Working Group 5 – International Rail Academic Network.

Qiuping Ma received the B.Sc. degree in Electronic Information Engineering from Sichuan Normal University (2013-2017), Chengdu, China, and Ph. D. degree in Electromagnetic Nondestructive Evaluation at the University of Electronic Science and Technology of China (UESTC), Chengdu, China. She is a postdoctoral researcher in UESTC now. Her research interests include smart sensors and system design for pipeline inspection.

Lawal Umar Daura (IEEE Member), an engineer and academic, holds both B.Eng. and M.Eng. degrees in Electrical Engineering from Bayero University Kano, Nigeria in 2005 and 2014. He earned his PhD in Electrical and Electronic Engineering from Newcastle University, UK in 2022, specializing in sensor technology for non-destructive testing and evaluation. He has demonstrated his unwavering commitment to his research, building a strong academic and research career, including a postdoctoral role as a Knowledge Transfer Partner (KTP) at Newcastle University. Currently, he holds a lecturer position in engineering at the University of Hertfordshire, UK. His research is focused on cutting-edge areas such as wireless power transfer for eddy-current testing, the development and application of Electromagnetic Acoustic Transducers (EMATs), and other electromagnetic sensors used in non-destructive testing and evaluation. Additionally, he has a keen interest in embedded electronic systems applications, contributing to the advancement of these technologies in various engineering fields.

Emmanuel Tashiwa Ibrahim received a B.Eng. in Electrical and Electronic Engineering from the Federal University of Technology, Yola, Adamawa State, Nigeria in 2004, and an M.Eng. in Electronic and Telecommunication Engineering from the University of Benin, Benin, Edo State, Nigeria in 2007. He is currently pursuing a Ph.D. degree in Electrical and Electronic Engineering with the School of Engineering at Newcastle University, U.K. He joined the Department of Electrical and Electronic Engineering at the University of Abuja in 2009 as an academic staff member. His primary research interest is electromagnetic sensing for nondestructive testing and evaluation (NDT&E).